

Yu, C., et al., 2023, Expanding the metamorphic devolatilization model: Komatiites as a source for orogenic gold deposits in high-grade metamorphic rocks: *Geology*, <https://doi.org/10.1130/G51446.1>

Supplemental Material

Table S1.

Figure S1–S2.

Supplemental Data S2 and S3.

Supplementary material

Methods

We conducted the thermodynamic simulation out using the HCh-based (Shvarov, 1999; Shvarov, 2008) HighPGibbs Gibbs minimization program (Zhong et al., 2020) that was developed to calculate fluid-rock equilibria at high pressures (up to ~55 kbar) using the DEW model (Sverjensky et al., 2014) and Davies activity coefficient equation (Davies, 1962) to describe aqueous species and solid solution models for metamorphic minerals. Calculations on the distribution of fluid species were carried out in the Au-Al-Ca-Cl-Fe-H-Mg-Na-O-Si system over 300–650 °C and 1–7 kbar for the basalt system, and 400–750 °C and 1–7 kbar for the komatiite system. Fluid-rock equilibrium calculations were conducted over the P-T grids with pressure intervals of 50 bar and temperature intervals of 2 °C.

At each P-T point, fluid-rock equilibrium was carried out using the “two-step” mode of HighPGibbs (Zhong et al., 2020): (i) at the first step, equilibrium between 100 kg of dry rock (basalt or komatiite) and excess solute-free pure water was calculated, to obtain the water contents that can just stabilize the hydrous metamorphic minerals at the given P-T; (ii) at the second step, minor amounts (0.5 kg) of H₂O-NaCl solution were added to the bulk metamorphic rock composition obtained from the first step, to obtain the composition, especially gold solubility, of the rock-buffered metamorphic fluid. The NaCl concentration of the fluid was set as 3 wt.% to simulate the typical low-salinity metamorphic fluid found in orogenic gold systems. The use of the two-step approach ensures that metamorphic fluids released at lower temperature will not remain in the system and interact with the rock at higher temperatures, and thus simulates the open system behavior of metamorphic devolatilization, i.e., metamorphic fluids episodically escaping from the

source rock as fluid pressure builds up.

Bulk rock compositions (Table S1) are based on greenstone belt samples compiled from the GEOROC database (<http://georoc.mpch-mainz.gwdg.de/georoc/>). Volcanic rocks from ten Archean Cratons were compiled, including Aldan Shield, Amazonian Craton, Baltic Shield, Dharwar Craton, Kaapvaal Craton, North Atlantic Craton, North China Craton, Sao Francisco Craton, Superior Province and West Australian Craton. The basaltic rock composition used for the modeling is taken from the average of the compiled samples with SiO₂ contents ranging from 45% to 52%, and the komatiite bulk composition was the average of samples with SiO₂ less than 45%. In addition, excess gold was added to the bulk rock compositions to determine the composition of native gold-saturated metamorphic fluid. Native gold is assumed to be the only gold-bearing mineral in the modeling. This assumption is made based on the fact that native gold or Au-Ag alloys are the major gold-bearing phases in ultramafic rocks or related Ni-Cu sulfide deposits, and pyrrhotite or other Fe-sulfides in these lithologies are characterized by low gold contents (Chen et al., 1993; Dare et al., 2010; Li et al., 2022; Melekestseva et al., 2013).

The aqueous species involved in simulations are listed in Table S2, and their thermodynamic properties are mainly from updated DEW database of Huang and Sverjensky (2019). Thermodynamic properties of aqueous Au species (AuHS, Au(HS)₂⁻, AuOH, Au(OH)₂⁻, AuCl, AuCl₂⁻) are modified from Pokrovski et al. (2014), by recalculating their pressure-dependent terms based on the empirical extrapolations proposed by Sverjensky et al. (2014). The thermodynamic data of rock-forming silicates, oxides and sulfides used in simulations are from Holland and Powell (1998), and that of native gold is from Barin and Platzki (1989) (Table S2). The mixing models for solid solutions are from Dale et al. (2005); Diener et al. (2007); Evans et al. (2010); Holland and

Powell (2003); Holland and Powell (1998); White et al. (2007) (Table S3).

Limitations of the simulations are as below: (i) The geochemistry of low-density fluids cannot be well described by the currently used fluid model, and thus large errors may exist in the simulation results at the high-temperature and low-pressures regimes. A density contour of 0.6 g/cm³ is shown in Figs. 1 and 2 of the main text, and results with higher fluid densities (to the upper left of the contours) are considered accurate. (ii) The activity coefficient of charged species cannot be accurately calculated if the ionic strengths of the fluids are beyond the limitation of the Davies extension of Debye-Hückel law (Davies, 1962), which are thought to be 0.5 (Bethke, 2008) or 0.7 molal (manual for GEM-Selector, available at <http://gems.web.psi.ch/TSolMod/doc/pdf/Activity-Coeffs.pdf>- accessed 6th April 2021). The ionic strength contours of 0.5 and 0.6 molal are shown in Figs. 1 and 2 of the main text, and simulation results to the lower pressure and higher temperature sides (lower right) of these contours are considered reliable. (iii) The mineral assemblages simulated by HighPGibbs are not as accurate as petrological tools such as THERMOCALC, because the simplified mineral models of HighPGibbs cannot describe the incompressibility and thermal expansion of metamorphic minerals. This limitation may lead to relatively large errors in calculating mineral assemblage at extreme pressures, but may not be significant in our simulation, which are only conducted up to 7 kbar.

Method References

Barin, I., and Platzki, G., 1989, Thermochemical data of pure substances, Wiley Online Library, v. 334.

Bethke, C. M., 2008, Geochemical and biogeochemical reaction modeling, New York, NY, USA,

Cambridge university press.

67 Chen, Y., Fleet, M., and Pan, Y., 1993, Platinum-group minerals and gold in arsenic-rich ore at the
68 Thompson mine, Thompson Nickel Belt, Manitoba, Canada: *Mineralogy and Petrology*, v. 49,
69 no. 1, p. 127–146.

70 Dale, J., Powell, R., White, R. W., Elmer, F. L., and Holland, T. J. B., 2005, A thermodynamic model for
71 Ca-Na clinoamphiboles in $\text{Na}_2\text{O}-\text{CaO}-\text{FeO}-\text{MgO}-\text{Al}_2\text{O}_3-\text{SiO}_2-\text{H}_2\text{O}-\text{O}$ for petrological
72 calculations: *Journal of Metamorphic Geology*, v. 23, no. 8, p. 771–791.

73 Dare, S. A., Barnes, S.-J., and Prichard, H. M., 2010, The distribution of platinum group elements (PGE)
74 and other chalcophile elements among sulfides from the Creighton Ni–Cu–PGE sulfide deposit,
75 Sudbury, Canada, and the origin of palladium in pentlandite: *Mineralium Deposita*, v. 45, no. 8,
76 p. 765–793.

77 Davies, C. W., 1962, *Ion Association*, Butterworths: London, UK.

78 Diener, J. F. A., Powell, R., White, R. W., and Holland, T. J. B., 2007, A new thermodynamic model for
79 clino- and orthoamphiboles in the system $\text{Na}_2\text{O}-\text{CaO}-\text{FeO}-\text{MgO}-\text{Al}_2\text{O}_3-\text{SiO}_2-\text{H}_2\text{O}-\text{O}$: *Journal*
80 *of Metamorphic Geology*, v. 25, no. 6, p. 631–656.

81 Evans, K. A., Powell, R., and Holland, T. J. B., 2010, Internally consistent data for sulphur-bearing phases
82 and application to the construction of pseudosections for mafic greenschist facies rocks in $\text{Na}_2\text{O}-$
83 $\text{CaO}-\text{K}_2\text{O}-\text{FeO}-\text{MgO}-\text{Al}_2\text{O}_3-\text{SiO}_2-\text{CO}_2-\text{O}-\text{S}-\text{H}_2\text{O}$: *Journal of Metamorphic Geology*, v. 28, no.
84 6, p. 667–687.

85 Holland, T. J. B., and Powell, R. T. J. B., 2003, Activity-composition relations for phases in petrological
86 calculations: an asymmetric multicomponent formulation: *Contributions to Mineralogy and*
87 *Petrology*, v. 145, no. 4, p. 492–501.

88 Holland, T. J. B., and Powell, R. T. J. B., 1998, An internally consistent thermodynamic data set for

89 phases of petrological interest: *Journal of metamorphic Geology*, v. 16, no. 3, p. 309–343.

90 Huang, F., and Sverjensky, D. A., 2019, Extended Deep Earth Water Model for predicting major element
91 mantle metasomatism: *Geochimica Et Cosmochimica Acta*, v. 254, p. 192–230.

92 Li, L., Sun, F., Li, B., Bai, Y., Wang, C., Qian, Y., Sun, Y., and Tan, S., 2022, Identification of
93 hydrothermal alteration and mineralization in the Sancha magmatic Cu-Ni-Au sulfide deposit,
94 NW China: Implications for timing and genesis of mineralization: *Ore Geology Reviews*, v. 143,
95 p. 104770.

96 Melekestseva, I. Y., Zaykov, V., Nimis, P., Tret'Yakov, G., and Tessalina, S., 2013, Cu-(Ni-Co-Au)-
97 bearing massive sulfide deposits associated with mafic-ultramafic rocks of the Main Urals Fault,
98 South Urals: Geological structures, ore textural and mineralogical features, comparison with
99 modern analogs: *Ore Geology Reviews*, v. 52, p. 18–36.

100 Pokrovski, G. S., Akinfiyev, N. N., Borisova, A. Y., Zotov, A. V., and Kouzmanov, K., 2014, Gold
101 speciation and transport in geological fluids: insights from experiments and physical-chemical
102 modelling: *Geological Society, London, Special Publications*, v. 402, no. 1, p. 9–70.

103 Shvarov, Y. V., 1999, Algorithmization of the numeric equilibrium modeling of dynamic geochemical
104 processes: *Geochemistry International*, v. 37, no. 6, p. 571–576.

105 Shvarov, Y. V., 2008, HCh: New potentialities for the thermodynamic simulation of geochemical systems
106 offered by windows: *Geochemistry International*, v. 46, no. 8, p. 834–839.

107 Sverjensky, D. A., Harrison, B., and Azzolini, D., 2014, Water in the deep Earth: The dielectric constant
108 and the solubilities of quartz and corundum to 60 kbar and 1200 °C: *Geochimica Et*
109 *Cosmochimica Acta*, v. 129, p. 125–145.

110 White, R. W., Powell, R., and Holland, T. J. B., 2007, Progress relating to calculation of partial melting

111 equilibria for metapelites: *Journal of Metamorphic Geology*, v. 25, no. 5, p. 511–527.

112 Zhong, R., Li, Y., Etschmann, B., Brugger, J., Yu, C., and Cui, H., 2020, HighPGibbs, a practical tool for

113 fluid-rock thermodynamic simulation in Deep Earth and its application on calculating nitrogen

114 speciation in subduction zone fluids: *Geochemistry Geophysics Geosystems*, v. 21, no. 5, p.

115 e2020GC008973.

116

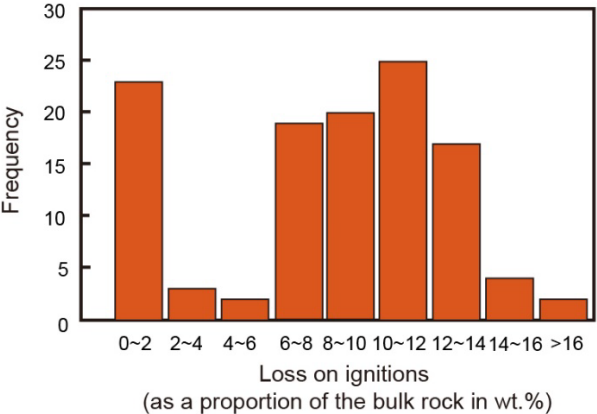


Fig. S1. Histogram showing loss on ignition, an approximation for bulk rock water content, of komatiites in global greenstone belts. Data are from the GEOROC database ([Supplemental Material File S3](#)).

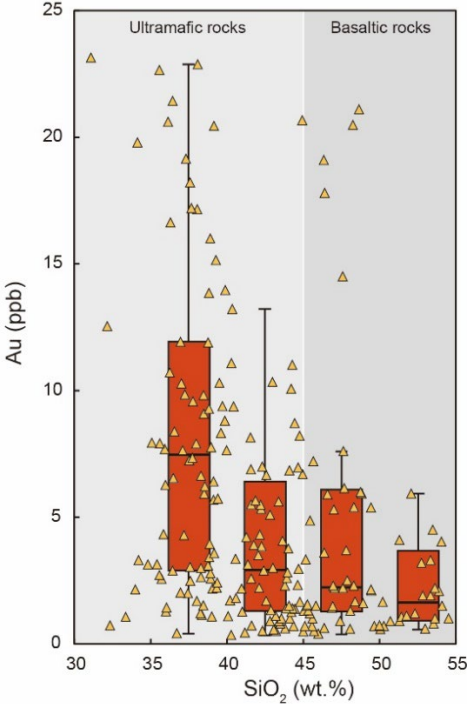


Fig. S2. Gold contents of volcanic rocks in Archean greenstone belts of the Yilgarn and Pilbara Cratons, showing the relationship with bulk rock SiO₂ content. Box-whisker plots show medians and quartiles of gold contents in volcanic rock with 35–40, 35–40, 40–45, 45–50 wt.% of SiO₂, respectively. Geochemical data are compiled from the GEOROC database ([Supplemental Material File S2](#)).

129 *Supplementary tables*

130 **Table S1. Bulk rock compositions used in the modelling (in wt.%)**

	Archean basaltic rock	Archean komatiite
SiO ₂	51.79	46.21
Al ₂ O ₃	14.75	4.25
MgO	7.81	33.86
FeO	9.91	7.09
Fe ₂ O ₃	2.87	4.49
CaO	10.45	4.10
Na ₂ O	2.32	
FeS ₂	0.19	0.19

131

132

133 **Table S2. Solid and aqueous species used in the modeling and sources of thermodynamic properties.**

Species	Reference	Species	Reference	Species	Reference
Native gold	Barin, 1989	O ₂ (aq)	Huang and Sverjensky, 2019	Na ⁺	Huang and Sverjensky, 2019
Hematite (Hm)	Holland and Powell, 1998	SiO ₂ (aq)	Huang and Sverjensky, 2019	NaOH(aq)	Huang and Sverjensky, 2019
Magnetite (Mt)	Holland and Powell, 1998	HSiO ₃ ⁻	Huang and Sverjensky, 2019	NaCl(aq)	Huang and Sverjensky, 2019
Pyrite (Py)	Holland and Powell, 1998	H ₂ S(aq)	Huang and Sverjensky, 2019	Mg ²⁺	Huang and Sverjensky, 2019
Paragonite (Pa)	Holland and Powell, 1998	HS ⁻	Huang and Sverjensky, 2019	MgOH ⁺	Huang and Sverjensky, 2019
Albite (Ab)	Holland and Powell, 1998	S ₂ ²⁻	Huang and Sverjensky, 2019	MgSO ₄ (aq)	Huang and Sverjensky, 2019
Quartz (Qt)	Holland and Powell, 1998	S ₂ O ₃ ²⁻	Huang and Sverjensky, 2019	MgCl ⁺	Huang and Sverjensky, 2019
Sillimanite (Sil)	Holland and Powell, 1998	SO ₂ (aq)	Huang and Sverjensky, 2019	Ca ²⁺	Huang and Sverjensky, 2019
Kyanite (Ky)	Holland and Powell, 1998	SO ₃ ²⁻	Huang and Sverjensky, 2019	CaOH ⁺	Huang and Sverjensky, 2019
Adalusite (Ad)	Holland and Powell, 1998	HSO ₃ ⁻	Huang and Sverjensky, 2019	CaSO ₄ (aq)	Huang and Sverjensky, 2019
Antigorite (Atg)	Holland and Powell, 1998	SO ₄ ²⁻	Huang and Sverjensky, 2019	CaCl ⁺	Huang and Sverjensky, 2019
Brucite (Br)	Holland and Powell, 1998	HSO ₄ ⁻	Huang and Sverjensky, 2019	CaCl ₂	Huang and Sverjensky, 2019
H ₂ O	Huang and Sverjensky, 2019	S ₃ ⁻	Huang and Sverjensky, 2019	Al ³⁺	Huang and Sverjensky, 2019
H ⁺	Huang and Sverjensky, 2019	HSO ₄ ⁻	Huang and Sverjensky, 2019	AlOH ²⁺	Huang and Sverjensky, 2019
OH ⁻	Huang and Sverjensky, 2019	Cl ⁻	Huang and Sverjensky, 2019	Al(OH) ₂ ⁺	Huang and Sverjensky, 2019
H ₂ (aq)	Huang and Sverjensky, 2019	HCl(aq)	Huang and Sverjensky, 2019	AlO ₂ ⁻	Huang and Sverjensky, 2019

134

135

$\text{HAlO}_2(\text{aq})$	Huang and Sverjensky, 2019	$\text{AuOH}(\text{aq})$	Revised from Pokrovski et al., 2014
Fe^{2+}	Huang and Sverjensky, 2019	$\text{Au}(\text{OH})_2^-$	Revised from Pokrovski et al., 2014
FeOH^+	Huang and Sverjensky, 2019	$\text{AuHS}(\text{aq})$	Revised from Pokrovski et al., 2014
FeCl^+	Huang and Sverjensky, 2019	$\text{Au}(\text{HS})_2^-$	Pokrovski et al., 2014, revised by DEW
FeCl_2	Huang and Sverjensky, 2019	$\text{AuCl}(\text{aq})$	Revised from Pokrovski et al., 2014
Fe^{3+}	Huang and Sverjensky, 2019	$\text{Au}(\text{Cl})_2^-$	Revised from Pokrovski et al., 2014
FeOH^{2+}	Huang and Sverjensky, 2019	-	
FeCl^{2+}	Huang and Sverjensky, 2019		
$\text{Na}(\text{HSiO}_3)$	Huang and Sverjensky, 2019		
$\text{Mg}(\text{HSiO}_3)^+$	Huang and Sverjensky, 2019		
$\text{FeO}(\text{aq})$	Huang and Sverjensky, 2019		
FeO^+	Huang and Sverjensky, 2019		
$\text{HFeO}_2(\text{aq})$	Huang and Sverjensky, 2019		
FeO_2^-	Huang and Sverjensky, 2019		
Au^+	Revised from Pokrovski et al., 2014		

Table S3. Solid solutions used in the modelling.

Mineral	End member	Formula	Activity model
Pyrrhotite (Po)	Troilite	FeS	Symmetrical
	Trov	Fe _{0.875} S	$W_{\text{troilite}} - W_{\text{trov}} = -3.19$
Chlorite (Chl)	Daphnite	Fe ₅ Al ₂ Si ₃ O ₁₀ (OH) ₄	Symmetrical
	Al-free chlorite	Mg ₆ Si ₄ O ₁₀ (OH) ₄	$W_{\text{daphnite}} - W_{\text{Al-free chlorite}} = 14.5$
	Amesite	Mg ₄ Al ₄ Si ₂ O ₁₀ (OH) ₄	$W_{\text{daphnite}} - W_{\text{amesite}} = 13.5$
	Clinochlore	Mg ₅ Al ₂ Si ₃ O ₁₀ (OH) ₄	$W_{\text{daphnite}} - W_{\text{clinochlore}} = 2.5$ $W_{\text{Al-free chlorite}} - W_{\text{amesite}} = 20$ $W_{\text{Al-free chlorite}} - W_{\text{clinochlore}} = 18$ $W_{\text{amesite}} - W_{\text{clinochlore}} = 18$
Actinolite (Act)	Tremolite	Ca ₂ Mg ₅ Si ₈ O ₂₂ (OH) ₂	Ideal
	Ferroactinolite	Ca ₂ Fe ₅ Si ₈ O ₂₂ (OH) ₂	
Hornblende (Hb)	Tremolite	Ca ₂ Mg ₅ Si ₈ O ₂₂ (OH) ₂	Symmetrical
	Tschermakite	Ca ₂ Mg ₃ Al ₄ Si ₆ O ₂₂ (OH) ₂	$W_{\text{Tremolite}} - W_{\text{glaucophane}} = 65$
	Pargasite	NaCa ₂ Mg ₄ Al ₃ Si ₆ O ₂₂ (OH) ₂	$W_{\text{tremolite}} - W_{\text{pargasite}} = 33$
	Glaucophane	Na ₂ Mg ₃ Al ₂ Si ₈ O ₂₂ (OH) ₂	$W_{\text{tremolite}} - W_{\text{tschermakite}} = 20$
	Ferroactinolite	Ca ₂ Mg ₅ Si ₈ O ₂₂ (OH) ₂	$W_{\text{tremolite}} - W_{\text{ferroactinolite}} = 10$ $W_{\text{glaucophane}} - W_{\text{pargasite}} = 50$ $W_{\text{glaucophane}} - W_{\text{tschermakite}} = 25$ $W_{\text{glaucophane}} - W_{\text{ferroactinolite}} = 39.3$ $W_{\text{pargasite}} - W_{\text{tschermakite}} = -38.5$ $W_{\text{pargasite}} - W_{\text{ferroactinolite}} = -1.9$ $W_{\text{tschermakite}} - W_{\text{ferroactinolite}} = 12.5$
Plagioclase (Pl)	Anorthite	CaAl ₂ Si ₂ O ₈	Symmetrical
	High albite	NaAlSi ₃ O ₈	$W_{\text{abh}} - W_{\text{an}} = 3.1$
Epidote (Ep)	Clinozoisite	Ca ₂ Al ₃ Si ₃ O ₁₂ (OH)	Symmetrical
	epidote	Ca ₂ FeAl ₂ Si ₃ O ₁₂ (OH)	
	Fe-epidote	Ca ₂ Fe ₂ AlSi ₃ O ₁₂ (OH)	
Olivine (Ol)	fayalite	Fe ₂ SiO ₄	Symmetrical
	forsterite	Mg ₂ SiO ₄	$W_{\text{fayalite}} - W_{\text{forsterite}} = 8$
Orthopyroxene (Opx)	enstatite	Mg ₂ Si ₂ O ₆	Symmetrical
	ferrosilite	Fe ₂ Si ₂ O ₆	$W_{\text{enstatite}} - W_{\text{ferrosilite}} = 7$
Anthophyllite (Anth)	Anthophyllite	Mg ₇ Si ₈ O ₂₂ (OH) ₂	Symmetrical
	Gedrite	Mg ₅ Al ₄ Si ₆ O ₂₂ (OH) ₂	$W_{\text{orthotremolite}} - W_{\text{anthophyllite}} = 45$
	Orthotremolite	Ca ₂ Mg ₅ Si ₈ O ₂₂ (OH) ₂	$W_{\text{orthotremolite}} - W_{\text{ferroanthophyllite}} = 75$
	ferroanthophyllite	Fe ₇ Si ₈ O ₂₂ (OH) ₂	$W_{\text{orthotremolite}} - W_{\text{gedrite}} = 70$
	Amoa1	Fe ₄ Mg ₃ Si ₈ O ₂₂ (OH) ₂	$W_{\text{orthotremolite}} - W_{\text{amoa1}} = 57$
	Amo2	Fe ₅ Mg ₂ Si ₈ O ₂₂ (OH) ₂	$W_{\text{orthotremolite}} - W_{\text{amoa2}} = 63$ $W_{\text{anthophyllite}} - W_{\text{ferroanthophyllite}} = 33$ $W_{\text{anthophyllite}} - W_{\text{gedrite}} = 25$ $W_{\text{anthophyllite}} - W_{\text{amoa1}} = 18$

			$W_{\text{anthophyllite}} - W_{\text{amoa2}} = 23$ $W_{\text{ferroanthophyllite}} - W_{\text{gedrite}} = 39.5$ $W_{\text{ferroanthophyllite}} - W_{\text{amoa1}} = 12$ $W_{\text{ferroanthophyllite}} - W_{\text{amoa2}} = 8$ $W_{\text{gedrite}} - W_{\text{amoa1}} = 29$ $W_{\text{gedrite}} - W_{\text{amoa2}} = 34.6$ $W_{\text{amoa1}} - W_{\text{amoa2}} = 20$
Talc (Tc)	talc	$\text{Mg}_3\text{Si}_4\text{O}_{10}(\text{OH})_2$	Ideal
	Fe-talc	$\text{Fe}_3\text{Si}_4\text{O}_{10}(\text{OH})_2$	

138

139

Table S4. Summary of names and ages of hypozonal gold deposits compiled for in Fig. 4 (after Kolb et al., 2015).

Deposit	Age
New Consort	3040 ± 84 Ma
Renco	2553 ± 114 Ma
Klein Lebata/Franke, and other smaller deposits	2660–2630 Ma
Hutti/Hira Buddini	2580–2540 Ma
The Granites	ca. 1795
Nevoria	2636 ± 1 Ma
Westonia	2650–2640 Ma
Southern Cross Province (Marvel Loch, Hopes Hill, Transvaal, Frasers, Corinthia)	ca. 2640 Ma
Coolgardie goldfield (Chalice, Three Mile Hill, Sand King)	2644 ± 8 Ma
Norseman region (Scotia)	>2620 ± 36 Ma
Lupin	≤2583 ± 9 Ma
Musselwhite	2690 ± 9 Ma
Fäboliden	ca. 1800 Ma
Svecofennian domain (Finland; Jokisivu, ca. 50 smaller deposits)	ca. 1840–1785 Ma
Navachab	525–520 Ma (Re–Os, molybdenite)